SAND2022-15986C

# Energy Storage Requirements for a Lunar DC Microgrid System

Wayne W. Weaver*, Rush D. Robinett III†
*Michigan Technological University, Houghton, MI, USA*

David G. Wilson ‡, Marvin Cook§, Jack Flicker¶
*Sandia National Laboratories, Albuquerque, NM, USA*

Joseph Young‖
*OptimoJoe, Houston, TX, USA*

Jeffrey T. Csank** , Marc A. Carbone††
*NASA Glenn Research Center, Cleveland, OH, USA*

## I. Introduction

The National Aeronautics and Space Administration's (NASA) Artemis program seeks to establish the first long-term presence on the Moon as part of a larger goal of sending the first astronauts to Mars. To accomplish this, the Artemis program is designed to develop, test, and demonstrate many of the technologies needed for deep space exploration and supporting life on another planet [1]. Long-term operations on the lunar base include habitation, science, logistics, and in-situ resource utilization (ISRU) [2]. This first phase of exploration will use current technologies, enabling NASA to develop new techniques and apply innovative approaches to solving problems in preparation for longer-duration missions far from Earth [3]. Future lunar mission success will heavily depend on the energy management of the lunar surface base-camp [4, 5]

To support the lunar surface base-camp, a microgrid may be considered as the power architecture. A microgrid is defined as a group of interconnected generation, loads and distributed energy resources within clearly defined electrical boundaries that acts as a single controllable entity with respect to the grid [6]. In this paper, a Lunar DC microgrid (LDCMG) structure can make up the backbone of energy distribution, storage, and utilization infrastructure [7, 8]. The environmental conditions of the lunar surface and its day-night cycle, with long periods of darkness, make the provision of energy a critical challenge [9]. Energy storage systems (ESS) are a critical component in the DC microgrid. However, standard system design techniques are driven by rule-of-thumb techniques which only account for local power balance requirements. An alternative method to analyze the LDCMG power distribution network and ESS design is the Hamiltonian surface shaping and power flow control (HSSPFC) [10] methodology. The Hamiltonian surface is a special type of Lyapunov function that can capture large-signal effects and accurately predict the stability boundaries [11] of the system at a wide range of timescales.

Furthermore, the HSSPFC methods can be used to generate exact requirements for an ESS given a system operating specification. For example, if a load and source profile is known and the DC bus voltage has a specified constraint, and the supervisory control system update rate is known, the HSSPFC can generate a set of requirements for the ESS. The ESS requirements can include total energy storage capacity, maximum power sourced (or sinked), as well as the frequency response [12, 13]. This ISRU system will include a networked three microgrid system which includes a Photo-voltaic (PV) array (generation) on one sub-microgrid and water extraction (loads) on the other two microgrids. A reduced-order model (ROM) of the system will be used to create a closed-form analytical model. Ideal ESS devices will be placed alongside each state of the ROM. The ideal ESS devices are used to determine the exact response needed to conform to a specific set of operating scenarios and system specifications. The system designer can then use outcomes from the ideal ESS devices to match actual ESS technologies, such as batteries, super-capacitors and/or flywheels.

*Professor, Mechanical Engineering - Engineering Mechanics, wwweaver@mtu.edu, AIAA Member
†Research Professor, Mechanical Engineering - Engineering Mechanics, rdrobine@mtu.edu, AIAA Associate Fellow
‡R&D Controls Engineer, Electrical Science & Experiments, dwilso@sandia.gov, AIAA Sr. Member
§R&D Computer Science Engineer, macook@sandia.gov, Non-Member
¶R&D Electrical Engineer, Non-Member
‖Chief Scientist, joe@optimojoe.com, Non-Member
**Electrical Engineer, Power Management and Distribution Branch, jeffrey.t.csank@nasa.gov, AIAA Sr. Member
††Electrical Engineer, marc.a.carbone@nasa.gov, Non-Member



Sandia National Laboratories is a multimission laboratory managed and operated by National Technology & Engineering Solutions of Sandia, LLC, a wholly owned subsidiary of Honeywell International Inc., for the U.S. Department of Energy's National Nuclear Security Administration under contract DE-NA0003525.

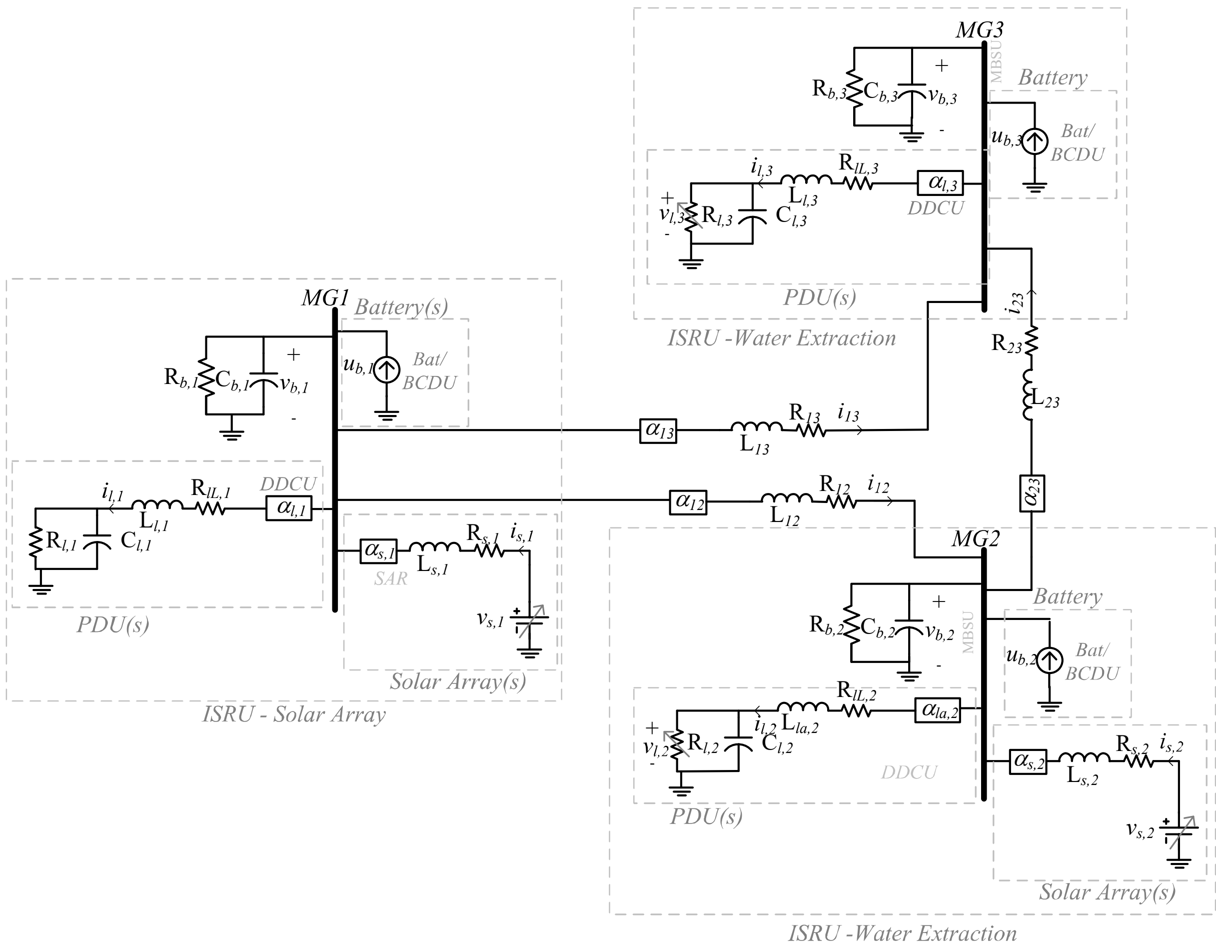


**Fig. 1 Reduced order model circuit.**

Further, by populating the entire system with ideal ESS devices, the HSSPFC method will also reveal the exact location of the required energy storage devices. It is common to show that many ideal ESS device locations show little to no utility. Therefore, the method reveals the optimal placement of the ESS within the LDCMG, capacity, and current response bandwidth.

## II. Reduced Order Model

A detailed model of the DC microgrid constructed MATLAB/Simulink is useful and effective to test the capabilities of the design as well as provides analysis tools for the overall performance. However, to properly derive the fundamental structure and performance of the system a ROM is needed such that it is written in a closed form for analytical analysis. For this study, the reduced order circuit model for LDCMG is shown in Fig. 1, which has three separate microgrids (MG1, MG2, and MG3) that are interconnected with tie lines.

In Fig. 1, MG1 represents the main ISRU-Solar Array, MG2 the a water extraction unit, but also includes a solar array, and MG3 represents another water extraction unit. However, it is important to point out that MG3 does not include a solar array source, so all power must come over the tie lines or from energy storage.

The model includes dc-to-dc converter units (DDCU) designated by the parameter $\alpha$. The DDCUs in this ROM are modeled as ideal, average-mode converters with the the model

$$v_a = \alpha v_b \tag{1}$$

$$i_b = \alpha i_a \tag{2}$$

where $\alpha$ is the conversion ratio, and the subscripts $a, b$ designate the port connections on the DDCU block. For this work the DDCUs are held to a two-quadrant operation where $\alpha > 0$ and are lossless. In the ROM model the power distribution units (PDU) are modeled as variable RLC loads behind controlled DDCU. For the study in this work the PDU in MG1 ($R_{l,1}$) is constant, but the PDUs in MG2 & 3 ($R_{l,2}$, $R_{l,3}$) are variable resistance. Therefore, the DDCU will regulate the load voltage and with a variable resistance the total power characteristic of the PDU approached a controlled variable power load.

Also shown in Fig. 1 are ESS that represent a battery. However, in the HSSPFC method for this ROM, the ESSs are modeled as a controlled current source, $u_b$. The HSSPFC method will reveal the performance required of the ESS to achieve a desired performance specification of the system. For this study, ESS devices have been placed only on the distribution bus of each microgrid. However, in a more general approach, an ESS can be placed on each state of the system, which could reveal a optimal ESS placement strategy when the ROM is analyzed.

The solar arrays in the ROM of Fig. 1 are modeled as a controlled voltage source ($v_s$) that represents the output of a PV array and power converter.

$$v_s = \begin{cases} v_{s,max} & \text{if } i_s < \frac{P_{s,max}}{v_{s,max}} \\ \frac{P_{s,max}}{i_s} & otherwise \end{cases} \tag{3}$$

where $P_{s,max}$ represents the maximum power output of the array and can be used to follow a solar irradiance pattern, and $v_{s,max}$ is a parameter that sets maximum output voltage of the PV converter. The PV model in Eq. (3) allows a reduced-order maximum power-point tracking behavior, but also enables a power output curtailment when the load does not match the supply.

The overall model of the ROM in Fig. 1 can be written in closed form as

$$\mathbf{M}\frac{\mathbf{dx}}{\mathbf{dt}} = \mathbf{Rx} + \mathbf{B^T u} + \mathbf{f}(\mathbf{x}, \mathbf{P_{s,max}}, t) = (\overline{\mathbf{R}} + \widetilde{\mathbf{R}})\mathbf{x} + \mathbf{B^T u} + \mathbf{f}(\mathbf{x}, \mathbf{P_{s,max}}, \mathbf{t}) \tag{4}$$

where $\mathbf{x^T}$ are the states, $\mathbf{f}$ are the nonlinear sources from Eq. (3), and $\mathbf{u^T}$ are the ideal ESS. Line impedance as well as power electronics conversion ratio $\alpha^{\mathbf{T}}$ are included in the impedance matrix $\mathbf{R}$. $\mathbf{R}$ has a special form that can be decomposed into a diagonal $\overline{\mathbf{R}}$ matrix and a skew symmetric $\widetilde{\mathbf{R}}$ matrix.

The power and energy of the ESS devices is important since it will be vital in the selection of the actual battery devices for the final design. The power from the ESS is found from

$$\mathbf{P_{ESS}} = \mathbf{u^T x}, \tag{5}$$

and the energy expended from the ESS is

$$\mathbf{W_{ESS}} = \int_0^t \mathbf{u^T x} dt \tag{6}$$

were $P_{ESS}$ and $W_{ESS}$ are vectors of power and energy for ESS at every state of the system. In this example, there are only 3 ESS devices on each of the LDCMG distribution buses.

The model shown in Fig. 1 has 14 states, so the full matrices of Eq. (13) would be cumbersome to display. However, as an illustration, the sub vectors and matrices for just MG1, without the cross microgrid tie line connections, are determined to be

$$\boldsymbol{x_1^T} = [i_{s,1} \;\; i_{l,1} \;\; v_{l,1} \;\; v_{b,1}] \tag{7}$$

$$\boldsymbol{u_1} = u_{b,1} \tag{8}$$

$$\boldsymbol{B_1^T} = [0 \;\; 0 \;\; 0 \;\; 1] \tag{9}$$

$$\boldsymbol{M_1} = \begin{bmatrix} L_{s,1} & 0 & 0 & 0 \\ 0 & L_{l,1} & 0 & 0 \\ 0 & 0 & C_{l,1} & 0 \\ 0 & 0 & 0 & C_{b,1} \end{bmatrix}, \tag{10}$$

$$\boldsymbol{R_1} = \begin{bmatrix} -R_{s,1} & 0 & 0 & -\alpha_{s,1} \\ 0 & -R_{lL,1} & -1 & \alpha_{l,1} \\ 0 & 1 & -1/R_{l,1} & 0 \\ \alpha_{s,1} & -\alpha_{l,1} & 0 & -1/R_{b,1} \end{bmatrix} \tag{11}$$

$$\mathbf{f_1}(\mathbf{x_1}, \mathbf{P_{s,1,max}}, t)^T = [v_{s,1}, 0, 0, 0] \tag{12}$$

where $v_{s,1}$ is taken from Eq. (3). MG2 has a similar form, and MG3 is similar except it would have only 3 states an $\mathbf{f_3}(\cdot, t) = 0$.

### A. Feed-Forward Control of the DDCUs

The feed-forward (FF) design of the HSSPFC method can be solved for the system for the desired reference values $\mathbf{x_{ref}}$ and $\frac{\mathbf{dx_{ref}}}{\mathbf{dt}}$, from

$$\mathbf{M}\frac{\mathbf{dx_{ref}}}{\mathbf{dt}} = \mathbf{R}\mathbf{x_{ref}} + \mathbf{B^T}\mathbf{u} + \mathbf{f}(\mathbf{x_{ref}}, \mathbf{P_{s,max}}, t). \tag{13}$$

The reference state vector $\boldsymbol{x_{ref}}$ contains the voltages and current of the system and the impedance matrix $\boldsymbol{R}$ contains the DDCU conversion ratios vector $\boldsymbol{\alpha}$. The reference values $\boldsymbol{x_{ref}}$ would come from a higher agent or optimization level control. However, For this paper the reference values are solved for a steady-state operation defined as

$$0 = \mathbf{R}\mathbf{x_{ref}} + \mathbf{B^T}\hat{\mathbf{u}} + \mathbf{f}(\mathbf{x_{ref}}, \mathbf{P_{s,max}}, t). \tag{14}$$

For the FF control the voltages in $\boldsymbol{x_{ref}}$ are defined as constant parameters, then Eq. (14) is solved for the currents of $\boldsymbol{x_{ref}}$ and the conversion ratios vector $\boldsymbol{\alpha}$. This FF solution is solved and the DDCU ratios $\boldsymbol{\alpha}$ are distributed to the system at a regular re-occurring update rate defined as $\tau$ min. The FF control implements a centralized optimization strategy for the steady-state operation of the model, but due to issues like communication channel bandwidth, it can only be solved and deployed every $\tau$ minutes. Note that the FF solution from Eq. (14) does not include ESS by design. In Eq. (14) the agent can also force a charge or discharge of the ESS devices by choosing a non-zero value for $\hat{\boldsymbol{u}}$. Otherwise, $\hat{\boldsymbol{u}}$ can be set to zero in which the FF solution assumes no ESS effort.

### B. FeedBack Control of the ESS

The ESS devices in the system are part of the feedback (FB) control strategy to actuate and regulate the system between FF update intervals, and in the cases when the PV array power output are insufficient to meet load demand. The FB control of the ESS uses the error states defined as

$$\tilde{\boldsymbol{x}} = \boldsymbol{x_{ref}} - \boldsymbol{x} \text{ and } \boldsymbol{\Delta u} = \boldsymbol{u_{ref}} - \boldsymbol{u}. \tag{15}$$

Then a local, servo-level proportional-integral (PI) control actuates the ESS with

$$\mathbf{u} = -\boldsymbol{k_p}\boldsymbol{B}\tilde{\boldsymbol{x}} - \boldsymbol{k_i}\boldsymbol{B}[\int_0^t \tilde{\boldsymbol{x}} d\tau], \tag{16}$$

where $\mathbf{k_p}$ and $\mathbf{k_i}$ are the FB gains, respectively. In this paper all FB controllers use the same gain values, but a system designer could choose different gains for different devices. Note that both $\mathbf{k_p}$ and $\mathbf{k_i}$ are selected as positive definite controller gains. The Hamiltonian or energy surface is the sum of kinetic and potential energies or

$$\mathcal{H} = \frac{1}{2}\tilde{\boldsymbol{x}}^T\boldsymbol{M}\tilde{\boldsymbol{x}} + \frac{1}{2}[\int_0^t \tilde{\boldsymbol{x}} d\tau]^T\boldsymbol{B}^T\boldsymbol{k_i}\boldsymbol{B}[\int_0^t \tilde{\boldsymbol{x}} d\tau] \quad \forall\tilde{\boldsymbol{x}} \neq \mathbf{0} \tag{17}$$

which is a positive definite function and defines the networked LDCMG *static stability condition*. The integral controller helps determine the ESS requirements necessary to shape/design the energy surface and guarantee *static stability*. The transient performance is determined from the rate of the Hamiltonian or the power flow constructed as

$$\dot{\mathcal{H}} = \tilde{\boldsymbol{x}}^T[\boldsymbol{M}(\dot{\boldsymbol{x}}_{\boldsymbol{ref}} - \dot{\boldsymbol{x}})] + \tilde{\boldsymbol{x}}^T\boldsymbol{B}^T\boldsymbol{k_i}\boldsymbol{B}[\int_0^t \tilde{\boldsymbol{x}} d\tau]. \tag{18}$$

Next substitute from both the state Eq. (4) and reference state Eq. (13) yields the *dynamic stability condition*

$$-\tilde{\boldsymbol{x}}^T[\boldsymbol{B}^T\boldsymbol{k_p}\boldsymbol{B} - \bar{\boldsymbol{R}}]\tilde{\boldsymbol{x}} < 0 \quad \forall\tilde{\boldsymbol{x}} \neq \mathbf{0}. \tag{19}$$

By selecting the proportional control gain, $\mathbf{k_p}$, determines the transient performance for the networked LDCMG system along the Hamiltonian energy surface. A full analysis of the FF and FB controls with stability and performance are included in [14, 15].

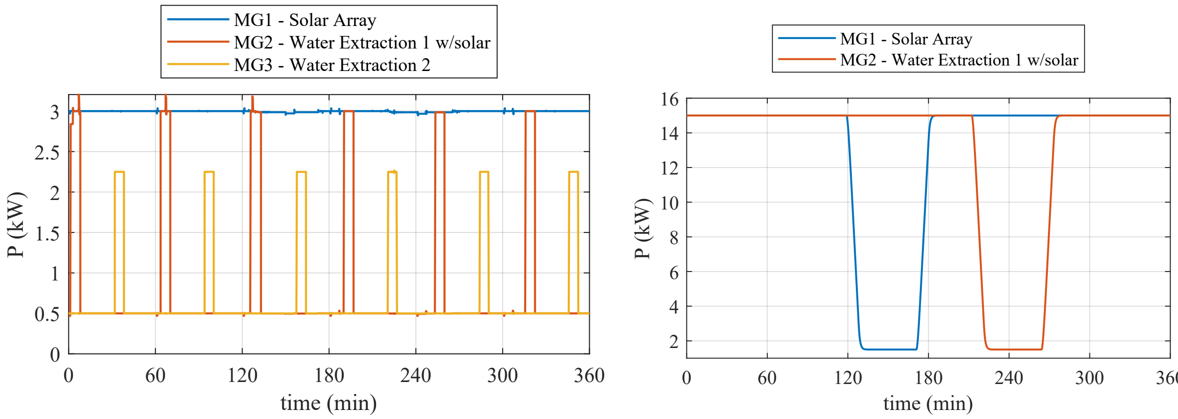


**(a) Load Power Profile**

**(b) PV Source Profile**

**Fig. 2 Vignette Profiles**

## III. Case Study Results

The LDCMG ROM shown in Fig. 1 with the FF and FB controls described in section II was programmed in MATLAB/Simulink. To demonstrate the ROM, a simple 6 hour scenario was constructed that illustrates three main features:

1) The FF and FB control can compensate for variations in PV outputs.
2) How the power from the PV and ESS is distributed between microgrids over the tie lines.
3) How the HSSPFC approach can help determine specifications and performance of the ESS devices.

The nominal operating voltage for each bus in the system is 300 $V_{dc}$ and each load has a nominal resistive load of 3 $kW$ for a total system wide load (2 loads per MG) up to 18 $kW$. Other general parameter values for this study are given in Table 1.

**Table 1 LDCMG ROM Parameters**

| Parameter | Symbol | Value |
|---|---|---|
| All Voltages Reference Set-points | v | 300 $V_{dc}$ |
| Nominal Restive Load | $R_b, R_l$ | 30 Ω |
| Nominal Load Power | $P_b, P_l$ | 3 $kW$ |
| Nominal Maximum PV Power | $P_{s,max}$ | 15 $kW$ |
| Inductance's | $L_s, L_l, L_{13}, L_{12}, L_{23}$ | 1 $mH$ |
| Inductor Resistance | $R_s, R_{iL}, R_{13}, R_{12}, R_{23}$ | 0.1 Ω |
| Capacitance's | $C_b, C_l$ | 1000 $\mu F$ |
| ESS FB Gains | $k_p, k_i$ | 0.1, 1 |

The vignette for this study is over a 6 hour period and the controllable loads on MG2 and MG2 pulse for 10 minutes every hour to simulate a Water Extraction operation when a mobile mining unit plugs into the microgrid to unload the extracted regolith an recharge its batteries. The load on MG1 remains constant. The load profiles are shown in Fig. 2a. Further, the vignette includes the impact of loss of PV power due to a *solar eclipse*. The maximum power from the PV arrays on MG1 and MG2 are shown in Fig. 2b, where the nominal max power for each array is 15 $kW$, but the PVs experiences 1 hour of loss starting at time 120 min for MG1 and 90 minutes later for MG2 starting at 210 minutes.

The model with profiles shown in Fig. 2 and FF/FB controls from section II was then simulated for 6 hours. For the results shown here the FF update rate $\tau$ was set to 1.5 minutes. The resulting FF conversion ratios for the PV arrays are shown in Fig. 3 and the resulting Power outputs from the two PV arrays are shown in Fig. 4. It is seen that when the

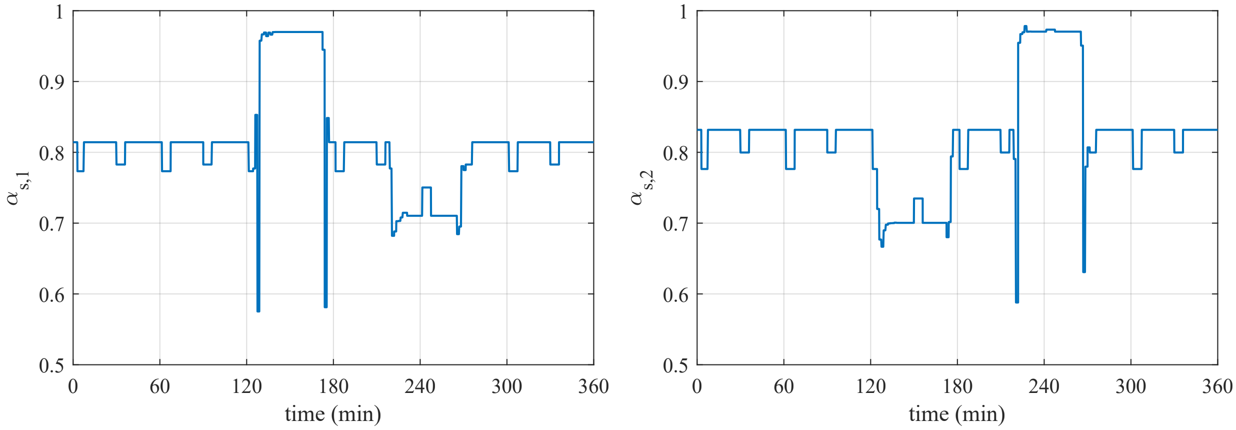


**(a) MG1 PV array** **(b) MG2 PV array**

**Fig. 3 PV array DDCU conversion ratios from FF solutions.**

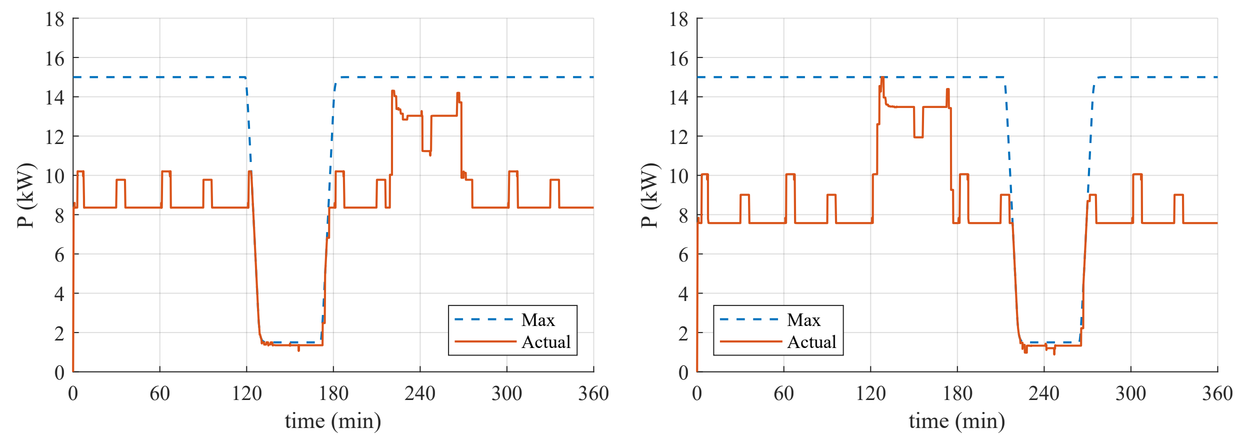


**(a) MG1 PV array** **(b) MG2 PV array**

**Fig. 4 PV array power limits and actual output.**

*solar eclipse* limits the power from MG1 at 120 min in Fig. 4(a), that the power from MG2 seen in Fig. 4(b) increases to meet demand. The same is true at 210 minutes when the *eclipse* hits MG2, then MG1 increases output. Further, it can be seen in Fig. 2 that the load pulses from MG2 and MG3 are being met by the PV arrays. It should also be pointed out that most of the time in Fig. 4 is it seen that the actual PV power output is less than the maximum. This indicates that power is being curtailed from the arrays because it is not needed to meet demand. However, a higher level agent optimizer could use this excess capability opportunity to recharge the ESS devises by setting a value for $\hat{\boldsymbol{u}}$ in the FF solution of Eq. (14).

The currents on the tie-lines between microgrids are shown in Fig. 5a. Since MG3 does not contain any PV array source, all of its power must be imported in over currents $i_{13}$, and $i_{23}$, hence these values are generally positive in Fig. 5a. However, since both MG1 and MG2 have PV array sources, the current between $i_{12}$ them remains, on average, low. When the 60 minute *eclipses* occurs at 120 min and 210 min, the tie line currents must be used to balance the load demand. In this example the current flow on all three tie-lines is mainly controlled with the converters $\alpha_{12}$, $\alpha_{13}$, and $\alpha_{23}$ shown in Fig. 1. However, if these converters were not included, the currents could still be controlled by deployment of the FF control solution, although perhaps not as precisely.

The LDCMG distribution bus voltages are show in Fig. 5b where it is seen that the voltages are regulated to the nominal value of 300 $V_{dc}$ with little noise ($\Delta V < 2$ %). This voltage ripple is mostly impacted by the PI gains described in section II.B. Higher values of $\mathbf{k_p}$ and $\mathbf{k_i}$ (given in Table 1) for each of the ESS FB regulators could improve the ripple.

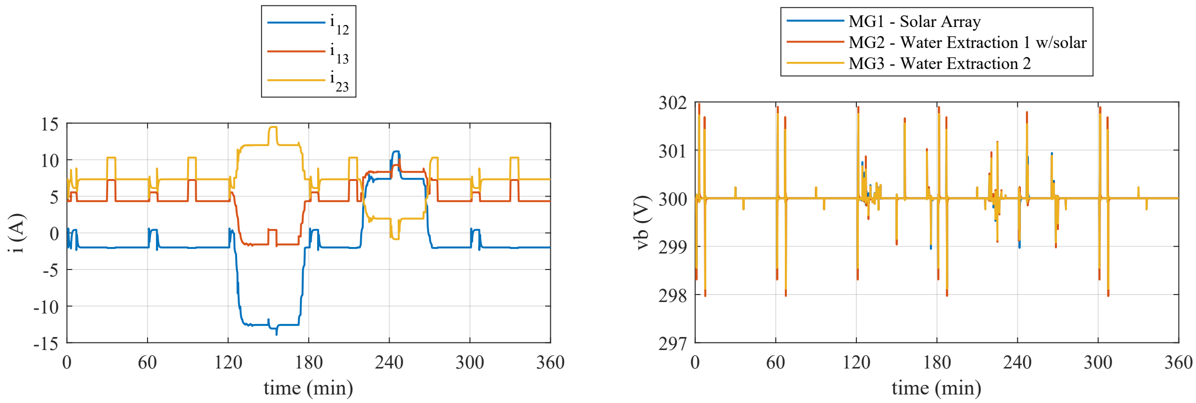


**(a) Cross MG line currents.** **(b) MG bus voltages.**

**Fig. 5 Bus voltages and line currents.**

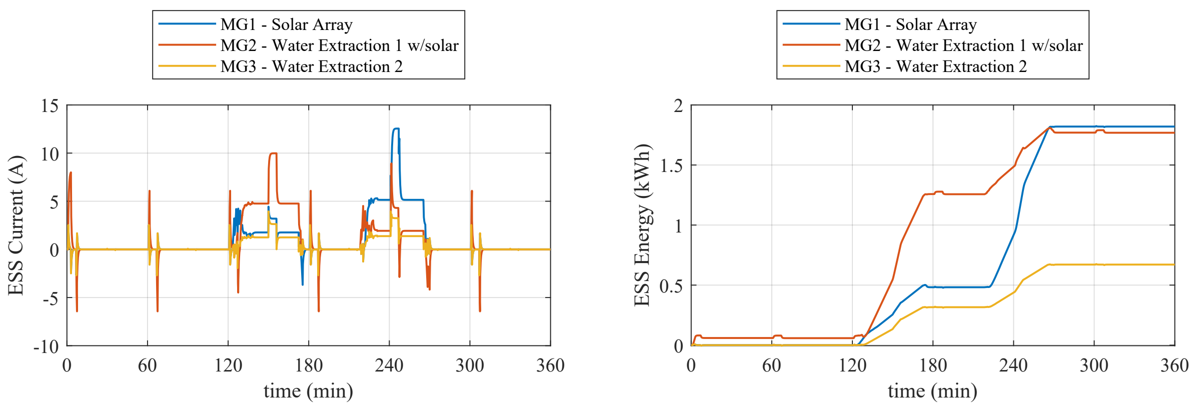


**(a) Bus ESS current $u_b$.** **(b) Bus ESS energy expended.**

**Fig. 6 ESS Effort**

Using the HSSPFC method, the stability of the system can be maintained, even with very large PI gains as described in [14].

The ESS devices on the LDCMG buses use the FB control strategy from section II.B between FF update intervals and in the case of PV supply deficiency. Fig. 6 shows the outputs from the bus ESS devices. Fig. 6a shows the ESS currents $\boldsymbol{u_b}$, and Fig. 6b shows the total energy expended from the ESS device as defined in Eq. (6) and converterd from units of Joules to kiloWatt-hours. Fig. 6b illustrates how the ESS device becomes more of a energy source during the *eclipses* in that the total energy output increases and does not re-charge after the 120 minute mark. However, as discussed earlier, a higher level agent control could use $\hat{\boldsymbol{u}}$ in the FF solution of Eq. (14) to re-charge the ESS devices after the *eclipses* when the maximum available PV power is higher than the actual used PV power as shown in Fig. 4. This re-charge operation could be used to ensure the net ESS energy over the vignette time horizon of 360 minutes is zero and the ESS is a storage device and not a net energy source. Nevertheless, Fig. 6b reveals the energy capacity that the particular ESS device must have to meet the needs of the vignette scenario. Further, the power from Fig. 5 can also help in the specification of the actual hardware selection for the final system design.

## IV. ESS specifications and FF Update Rate

The simulation example results given in section III illustrate the response of the ROM model with FB control and the FF control. The solutions of the FF control are distributed to the DDCU converters, with $\alpha$ conversion ratios, at $\tau = 1.5$ *min* intervals. The update rate interval $\tau$ can represent the bandwidth at which a centralized or agent based

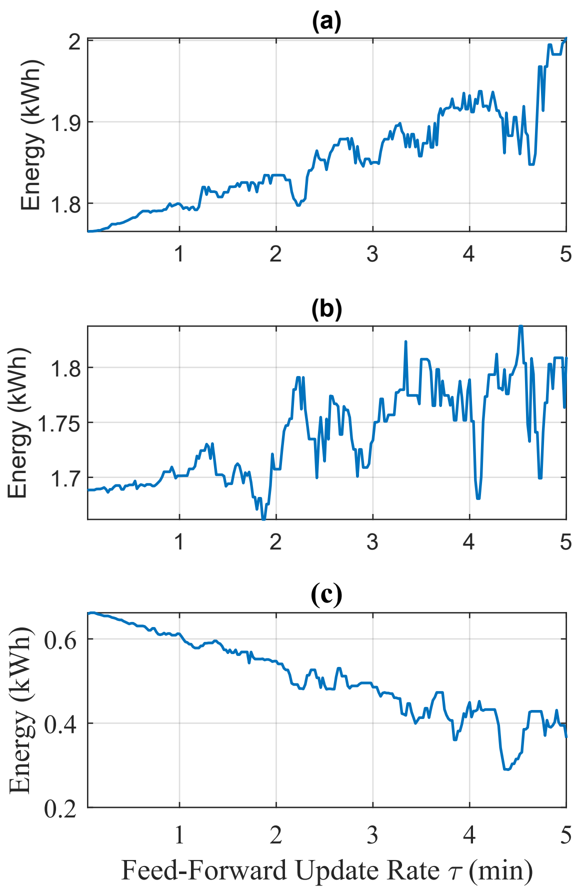


**Fig. 7 Bus ESS device required energy capacity for $\tau$ update rate. (a) MG1, (b) MG2, (c) MG3.**

control level can communicate with the system components. The update interval $\tau$ can have a significant impact on the performance and design specifications of the ESS and system. This section of the paper will show the results of a batch study of simulations for the same system and parameters given in section III, but with $\tau$ swept over a range from $0.1\ min < \tau < 5\ min$ in 0.01 *min* steps. A total of 490 simulations were conducted and the resulting data compiled. For this study all FF solutions are distributed simultaneously on the same interval $\tau$, however, it would be feasible to have different update rates for the DDCU converter ratios.

One important impact that the value of $\tau$ has is the total energy capacity of the ESS devices. For each simulation run the maximum value was taken from the ESS energy results. For example the maximum values of energy show in Fig. 6b is the data point when $\tau = 1.5\ min$. The resulting data is shown in Fig. 7. It is seen in Fig. 7(a)&(b) that as $\tau$ increases the general trend for energy in MG1 and MG2 also increase, but in Fig. 7(c) the energy capacity goes down. This is likely due to the fact that MG3 does not have a PV array and does not experience the *eclipse* seen in MG1 and MG2. The ESS on bus MG3 does not need to act as a primary source at any point and larger values of $\tau$ for MG3. Conversely, as the update rate increases the ESS on MG1 and MG2 have to provide primary power for longer periods during the *eclipses* and therefore the total energy capacity increases for those devices. Further it is seen in Fig. 7 that local minimums exist in all three energy capacity plots that indicates that potentially, given the proper selection of $\tau$ a smaller ESS, likely a battery, could be selected for the device in that location.

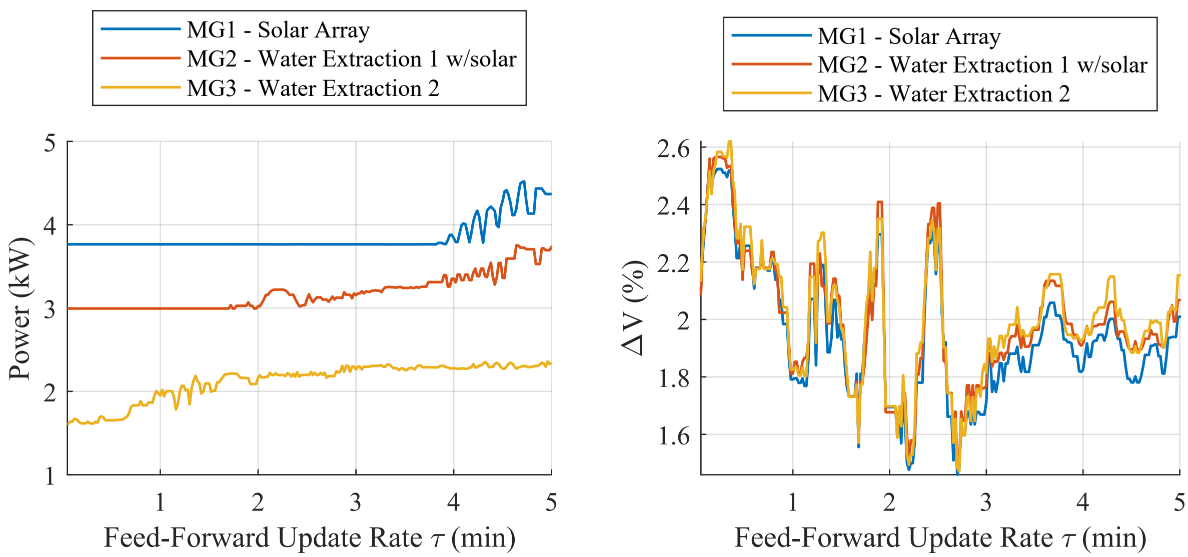


**(a) Maximum power output.**

**(b) Maximum bus voltage ripple for $\tau$ update rate.**

**Fig. 8 ESS performance for batch study with $\tau$ update rate.**

Total ESS energy capacity is important in the selection of the update rate $\tau$, but there are other factors to consider as well. The update interval $\tau$ also impact the power output of the ESS where the power is defined in Eq. (5). The maximum power of the bus ESS devices is shown in Fig. 8a, where it is seen that for lower values of $\tau$ the max power from MG1 and MG2 remain constant until the duration of $\tau$ is large enough that the ESS has to expend more power to regulate the system due to the *eclipses* and load pulse profiles. Further, the ripple, or noise on the voltages of the LDCMG can also be an important design factor. Fig. 8b shows the percent voltage ripple (peak-to-peak) of the 300 $V_{dc}$ buses. In Fig. 8b it is seen that the ripple is a minimum when $\tau \approx 2.6\ min$. However, it is important to point out that all ripple values in this data are well below industry standards and are also impacted significantly by the choice of PI gains in the FB control of section II.B.

## V. Conclusions

This paper has given an overview of the reduced-order modeling and methods used to drive the optimal ESS requirements of an LDCMG. The method used is the HSSPFC which formulates the system with ideal FB control that drives the ESS devices and determines FF power converter actuation. The HSSPFC method is a powerful tool that defines the exact nature of the ESS devices and locations in the system to achieve system and device requirements and specifications for a given operational scenario. A six hour vignette scenario was used to illustrate the operation, which includes solar *eclipses* that limit the PV array power, as well as pulsed load demands. This example illustrates the role and efforts that the ESS and DDCU devices play in regulating the system and provide performance specifications for ESS devices and the deployed FF optimal set-points of the DDCU. A batch simulation study was conducted which shows how the performance would change for different FF update rates.

## VI. Acknowledgment

This article has been authored by an employee of National Technology  Engineering Solutions of Sandia, LLC under Contract No. DE-NA0003525 with the U.S. Department of Energy (DOE). The employee owns all right, title and interest in and to the article and is solely responsible for its contents. The United States Government retains and the publisher, by accepting the article for publication, acknowledges that the United States Government retains a non-exclusive, paid-up, irrevocable, world-wide license to publish or reproduce the published form of this article or allow others to do so, for United States Government purposes. The DOE will provide public access to these results of federally sponsored research in accordance with the DOE Public Access Plan https://www.energy.gov/downloads/doe-public-access-plan.

## References

[1] Smith, M., Craig, D., Herrmann, N., Mahoney, E., Krezel, J., McIntyre, N., and Goodliff, K., "The Artemis program: an overview of NASA's activities to return humans to the moon," *2020 IEEE Aerospace Conference*, IEEE, 2020, pp. 1–10.

[2] Creech, S., Guidi, J., and Elburn, D., "Artemis: An Overview of NASA's Activities to Return Humans to the Moon," *2022 IEEE Aerospace Conference (AERO)*, IEEE, 2022, pp. 1–7.

[3] Aaseng, G., Frank, J., Iatauro, M., Knight, C., Levinson, R., Ossenfort, J., Scott, M., Sweet, A., Csank, J., Soeder, J., et al., "Development and testing of a vehicle management system for autonomous spacecraft habitat operations," *AIAA Space Forum*, 2018.

[4] Csank, J. T., Soeder, J. F., Carbone, M. A., Granger, M. G., Tomko, B. J., Muscatello, M. J., and Follo, J. C., "A Control Framework for Autonomous Smart Grids for Space Power Applications," *International Astronautical Congress (IAC)*, 2019.

[5] Colozza, A. J., "Small lunar base camp and in situ resource utilization oxygen production facility power system comparison," Tech. Rep. E-19754, 2020.

[6] Lasseter, B., "Microgrids [distributed power generation]," *IEEE power engineering society winter meeting*, Vol. 1, IEEE, 2001, pp. 146–149.

[7] Flicker, J. D., "Robust Autonomous and Fault-tolerant DC Microgrid Development for Long-Term Lunar Habitation." Tech. rep., Sandia National Lab.(SNL-NM), Albuquerque, NM (United States), 2021.

[8] Saha, D., Bazmohammadi, N., Raya-Armenta, J. M., Bintoudi, A. D., Lashab, A., Vasquez, J. C., and Guerrero, J. M., "Space microgrids for future manned lunar bases: A review," *IEEE Open Access Journal of Power and Energy*, 2021.

[9] Palos, M. F., Serra, P., Fereres, S., Stephenson, K., and González-Cinca, R., "Lunar ISRU energy storage and electricity generation," *Acta Astronautica*, Vol. 170, 2020, pp. 412–420.

[10] Robinett III, R. D., and Wilson, D. G., *Nonlinear Power Flow Control Design: Utilizing Exergy, Entropy, Static and Dynamic Stability, and Lyapunov Analysis*, Springer Science & Business Media, 2011.

[11] Weaver, W. W., Robinett, R. D., Wilson, D. G., and Matthews, R. C., "Metastability of pulse power loads using the hamiltonian surface shaping method," *IEEE Transactions on Energy Conversion*, Vol. 32, No. 2, 2017, pp. 820–828.

[12] Bijaieh, M. M., Weaver, W. W., and Robinett, R. D., "Energy storage requirements for inverter-based microgrids under droop control in dq coordinates," *IEEE Transactions on Energy Conversion*, Vol. 35, No. 2, 2019, pp. 611–620.

[13] Weaver, W. W., Bijaieh, M. M., Robinett, R. D., and Wilson, D. G., "Energy storage baseline requirements for pulsed power loads," *2019 IEEE Electric Ship Technologies Symposium (ESTS)*, IEEE, 2019, pp. 52–59.

[14] Weaver, W. W., Robinett, R. D., Parker, G. G., and Wilson, D. G., "Distributed control and energy storage requirements of networked Dc microgrids," *Control Engineering Practice*, Vol. 44, 2015, pp. 10–19.

[15] Wilson, D. G., Robinett, R. D., Weaver, W. W., Byrne, R. H., and Young, J., "Nonlinear power flow control design of high penetration renewable sources for ac inverter based microgrids," *2016 international symposium on power electronics, electrical drives, automation and motion (speedam)*, IEEE, 2016, pp. 701–708.